Structures and Mechanisms of the Northward Propagating Boreal Summer Intraseasonal Oscillation*

XIANAN JIANG, TIM LI,[+] AND BIN WANG[+]

Department of Meteorology, School of Ocean and Earth Science and Technology, University of Hawaii at Manoa, Honolulu, Hawaii

ABSTRACT

The spatial and temporal structures of the northward-propagating boreal summer intraseasonal oscillation (BSISO) are revealed based on the analysis of both the ECHAM4 model simulation and the NCEP–NCAR reanalysis. The BSISO structure and evolution characteristics simulated by the model bear many similarities to those derived from the NCEP–NCAR reanalysis. The most notable features are the remarkable meridional asymmetries, relative to the BSISO convection, in the vorticity and specific humidity fields. A positive vorticity perturbation with an equivalent barotropic structure appears a few latitude degrees north of the convection center. The maximum specific humidity also shows a clear northward shift in the lower troposphere.

Two internal atmospheric dynamics mechanisms are proposed to understand the cause of the northward propagation of the BSISO. The first is the vertical shear mechanism. The key process associated with this mechanism is the generation of barotropic vorticity due to the coupling between the free-atmosphere baroclinic and barotropic modes in the presence of the vertical shear of the mean flow. The induced barotropic vorticity in the free atmosphere further causes a moisture convergence in the planetary boundary layer (PBL), leading to the northward shift of the convective heating. The second mechanism is the moisture–convection feedback mechanism. Two processes contribute to the northward shift of the low-level moisture. One is the moisture advection by the mean southerly in the PBL. Another is the moisture advection by the BSISO wind due to the mean meridional specific humidity gradient. The asymmetric specific humidity contributes to the northward shift of the convective heating.

A theoretical framework is constructed to investigate the instability of the northward-propagating BSISO mode and the relative roles of various mechanisms including air–sea interactions. An eigenvalue analysis indicates that the northward propagation of the BSISO is an unstable mode of the summer mean flow in the monsoon region. It has a typical wavelength of 2500 km. While the easterly shear contributes to the northward propagation primarily north of 5°N, the moisture feedback and the air–sea interaction also contribute significantly, particularly in the region near and south of the equator. The internal atmospheric dynamics are essential in causing the northward propagation of the BSISO over the tropical Indian Ocean.

1. Introduction

The intraseasonal oscillation (ISO) is one of the most significant signals in the tropical atmosphere. The pioneering work by Madden and Julian (1971) first detected the ISO signal, with a period of 40–50 day, in the zonal wind field over Canton Island. Later they further documented the spatial structure of the ISO based on pressure and wind fields (Madden and Julian 1972)

Corresponding author address: Dr. Tim Li, Dept. of Meteorology, SOEST, University of Hawaii at Manoa, 2525 Correa Road, POST 409B, Honolulu, HI 96822.
E-mail: timli@hawaii.edu

and found that this oscillation is of global scale and is characterized primarily by equatorial eastward propagation with a zonal wavenumber-1 structure.

While the strong eastward propagating ISO (the Madden–Julian mode) is primarily observed in boreal winter, the ISO in boreal summer is dominated by northward propagation in the Indian sector and northwestward propagation off the equator in the western Pacific. Yasunari (1979, 1980) was among the first to document the marked northward movement of clouds and convection associated with the ISO from the equatorial zone to around 30°N over the South Asian monsoon region. The fluctuation of this mode is associated with major "active" and "break" cycles of the Indian monsoon. Yasunari noticed that the northward movement was initiated by eastward-propagating cloud disturbances developing over the equatorial Indian Ocean.

This northward propagating mode with the 30–50-day period was further documented by other studies using various meteorological variables (e.g., Sikka and

Gadgil 1980; Krishnamurti and Subrahmanyam 1982; Murakami et al. 1984; Lorenc 1984; Cadet 1986; Lau and Chan 1986; Wang and Rui 1990). Sikka and Gadgil (1980) pointed out that during boreal summer there are two maximum cloud zones (MCZ) over the Indian longitudes (70°–90°E), one being along 15°N and the other near the equator. The two convection zones exhibit a seesaw characteristic, that is, the equatorial MCZ is present while the other one is absent, or vice versa. Most interestingly, the active/break cycle of the monsoon MCZ is closely connected to the northward propagation of the equatorial MCZ. Krishnamurti and Subrahmanyam (1982) noted a steady meridional propagation of a train of troughs and ridges that form near the equator and dissipate near the foot of Himalayas over the Indian subcontinent sector. The meridional length scale of this mode is about 3000 km, and its meridional phase speed is about 0.75° latitude per day.

By analyzing 10-yr (1975–85) pentad mean OLR data, Wang and Rui (1990) classified the ISO events into three categories: eastward propagation (65%), independent northward propagation (20%), and westward propagation (15%). The eastward-propagation mode, which is trapped near the equator, is more active in boreal winter than in summer. The independent northward propagation, which is not associated with the eastward propagation, is found over Indian and western Pacific monsoon regions in boreal summer from May to October. For the eastward propagating mode, a special scenario is identified in which the northward propagation is associated with the eastward propagation along the equator. Among the total northward-propagating cases over the Indian and western Pacific regions during the boreal summer, about half of them are independent northward propagation cases, and the other half seem to be connected with eastward propagating convection along the equator.

The aforementioned observational studies indicate that the northward propagation is one of the most striking features of the boreal summer ISO (BSISO) in the Asian monsoon region. An open question is what causes the northward propagation of the BSISO convection in the monsoon region. Webster (1983) hypothesized that the land surface heat flux into the atmospheric planetary boundary layer (PBL) may play a role in destabilizing the atmosphere ahead of the convection, leading to a northward shift of the convective zone. However, observations show that the strongest northward propagation signal appears over the northern Indian Ocean (along Bay of Bengal longitudes), not over the land. Goswami and Shukla (1984) proposed that the convection–thermal relaxation feedback might be a key for generating a standing oscillation between the equatorial and monsoon MCZs. In their hypothesis, convective activity results in an increase of static stability, which depresses convection itself; meanwhile, dynamical and radiative relaxation decreases moist static stability and brings the atmosphere to a new convectively unstable

state. However, they did not address the mechanism associated with the northward propagation of the ISO.

Based on simulations from an intermediate atmospheric model, Wang and Xie (1997) proposed a Rossby wave emanation hypothesis as follows. When the convection moves eastward to the central equatorial Pacific, the reduction of the mean SST and specific humidity leads to the emanation of Rossby waves from the equatorial convection, which forms a ''convection front.'' This convection front tilts northwestward from the equator to 20°N (a V shape), resulting in an apparent northward movement as the entire wave packet migrates eastward. This Rossby wave emanation hypothesis was supported by Lawrence and Webster (2002), who showed that a large portion of the northward propagation is connected to the eastward moving component in their wavenumber–frequency analysis maps. However, this Rossby wave emanation hypothesis does not explain the independent northward propagating ISOs.

The interaction between the atmosphere and ocean is another possible mechanism contributing to the northward propagation. This is because reduced surface latent heat fluxes (due to a decrease in the total wind speed) may increase sea surface temperature (SST) to the north of the convection, leading to a moisture convergence in the PBL (Kemball-Cook and Wang 2001). Thus the atmosphere north of the convection is destabilized, and the convection moves northward. While observational data confirm the SST–convection phase relationship, it is not clear whether the air–sea interaction plays an active role in the northward propagation or the SST is simply a passive response to the atmospheric forcing.

The goal of this study is to reveal essential atmospheric dynamical processes that give rise to the northward propagation of the BSISO. The specific scientific questions to be addressed are as follows. What is the meridional phase relationship among various meteorological variables for the northward propagating ISO mode? What causes the meridional phase relationship? Why is the northward propagation favorable over the South Asian and western Pacific monsoon regions? What is the relative role of the internal atmospheric dynamics and air–sea interaction in contributing to the northward propagation?

To achieve this goal, we rely on the analysis from both atmospheric general circulation model (AGCM) simulations (in which we exclude the effect of air–sea interactions by specifying climatological monthly mean SST) and observations. In section 2, a brief description of the model and the observational data is given. In section 3, the temporal and spatial structures of the northward moving ISO mode are constructed based on both the AGCM simulations and the observations. The analysis of the BSISO structures leads to the discovery of two new mechanisms, which are discussed in section 4. In section 5, we further advance a simple theoretical framework to explore the instability nature of the northward propagating BSISO mode and to understand the

relative role of various mechanisms including the air–sea interaction in contributing to the northward propagation. Finally, a summary is given in the last section.

2. Model and data

The model used in this study is the ECHAM AGCM version 4.0 (Roeckner et al. 1996) at a resolution of T30 and 19 vertical levels. The convection scheme used in this AGCM is the mass flux scheme for penetrative, shallow, and midlevel convection (Tiedtke 1989) modified by Nordeng (1994) so that the cloud-base mass flux is linked to convective instability for the penetrative convection. This model is integrated for 15 years, with the lower boundary condition given by the climatological monthly mean SST. Daily averaged fields are written out for analysis.

To check the reliability of the model simulation, we analyze the National Centers for Environmental Prediction–National Center for Atmospheric Research (NCEP–NCAR) reanalysis dataset for comparison. Again, daily averaged data are used for a period from 1980 to 2001, and the horizontal resolution of the reanalysis data is 2.5° latitude × 2.5° longitude and vertically there are 12 pressure levels. The 3D variables include the zonal and meridional wind components, vertical p velocity, and specific humidity. The daily averaged outgoing longwave radiation (OLR) data from the National Oceanic and Atmospheric Administration is employed as the proxy for convection. To compare the model precipitation with the observed, the Climate Prediction Center (CPC) Merged Analysis of Precipitation data (CMAP; Xie and Arkin 1997) are used.

To isolate the ISO signal, a bandpass filtering method is applied. For daily data, harmonics between 4 and 24 are extracted each year, which corresponds to the period of 15–90 days. This time filtering is applied to each meteorological field for both the model output and the NCEP–NCAR reanalysis.

3. BSISO structures as revealed from the AGCM and reanalysis data

Before revealing the ISO structure, we first examine the model performance in the mean monsoon simulation in boreal summer. Figure 1 shows the observed and simulated climatological summer mean precipitation and wind fields. The model captures the gross pattern of the summer rainfall such as the rainfall centers around Philippine and the South China Sea and over the equatorial Indian Ocean. The model, however, underestimates the rainfall amount over the Bay of Bengal but overestimates it over the equatorial Indian Ocean. The most notable circulation features in boreal summer over the south Asian monsoon region are the gigantic anticyclonic circulation over the Asian continent and prevailing easterlies in the upper troposphere and the cross-equatorial Somali jet and westerlies in the lower tro-

posphere. These features are well reproduced by the ECHAM AGCM. As will be discussed later, this pronounced vertical shear of the mean flow plays an important role for the amplification and northward propagation of the BSISO mode.

The meridional phase propagation of the BSISO mode may be readily identified by a Hovmöller diagram of the rainfall along 70°–95°E during a 15-yr integration period (Fig. 2). Note that the northward propagation is most pronounced during the boreal summer each year. The propagation also exhibits strong interannual variability. More or stronger northward propagation events appear in some years while less or weaker events appear in other years. Interannual variability results from internal atmospheric dynamics as the climatological monthly mean SST are specified. During the boreal winter, the rainfall tends to move southward. Both the northward and southward propagations start from the equatorial region.

To reveal the meridional and vertical structure of the BSISO, we take a composite approach by selecting 23 strong northward propagation cases. The composite is constructed as such that at day 0 the ISO convection arrives exactly at 5°N along 70°–95°E. The time sequence of the composite rainfall from day −16 to 12 (with a 2-day interval) is illustrated in Fig. 3. At day −16, an ISO convection center is located in the equatorial western Indian Ocean (about 60°E), and the intensity of the convection is weak. In the ensuing days, the convection intensifies and moves eastward along the equator. At day −8, the maximum rainfall center arrives in the eastern equatorial Indian Ocean around 90°E. After that, the convection starts to move northward, and at the same time it intensifies. At day 4, the convection arrives at 10°N and reaches maximum intensity. Later it begins to weaken while continuing to move northward. At day 10, the convection center arrives in the northern Bay of Bengal.

Of particular interest is the generation of a negative rainfall center over the western equatorial Indian Ocean at day −2 when the convection in the eastern Indian Ocean moves to 3°N. Later, this negative convection anomaly amplifies and moves eastward to the eastern equatorial Indian Ocean and then moves northward, following the behavior of the previous convection. This poses a possible scenario for the origin of the BSISO, that is, the BSISO, as an unstable mode of the summer mean flow, is self-regulated within the monsoon region. We will discuss this issue further in section 5.

After the convection is initiated over the western equatorial Indian Ocean and moves eastward to the eastern equatorial Indian Ocean around 90°E, there is no clear eastward moving convection signal beyond east of this longitude. This implies that the composite above mainly captures the independent northward propagating ISO mode.

The meridional phase speed of the BSISO may be estimated from the time–latitude section of the com-
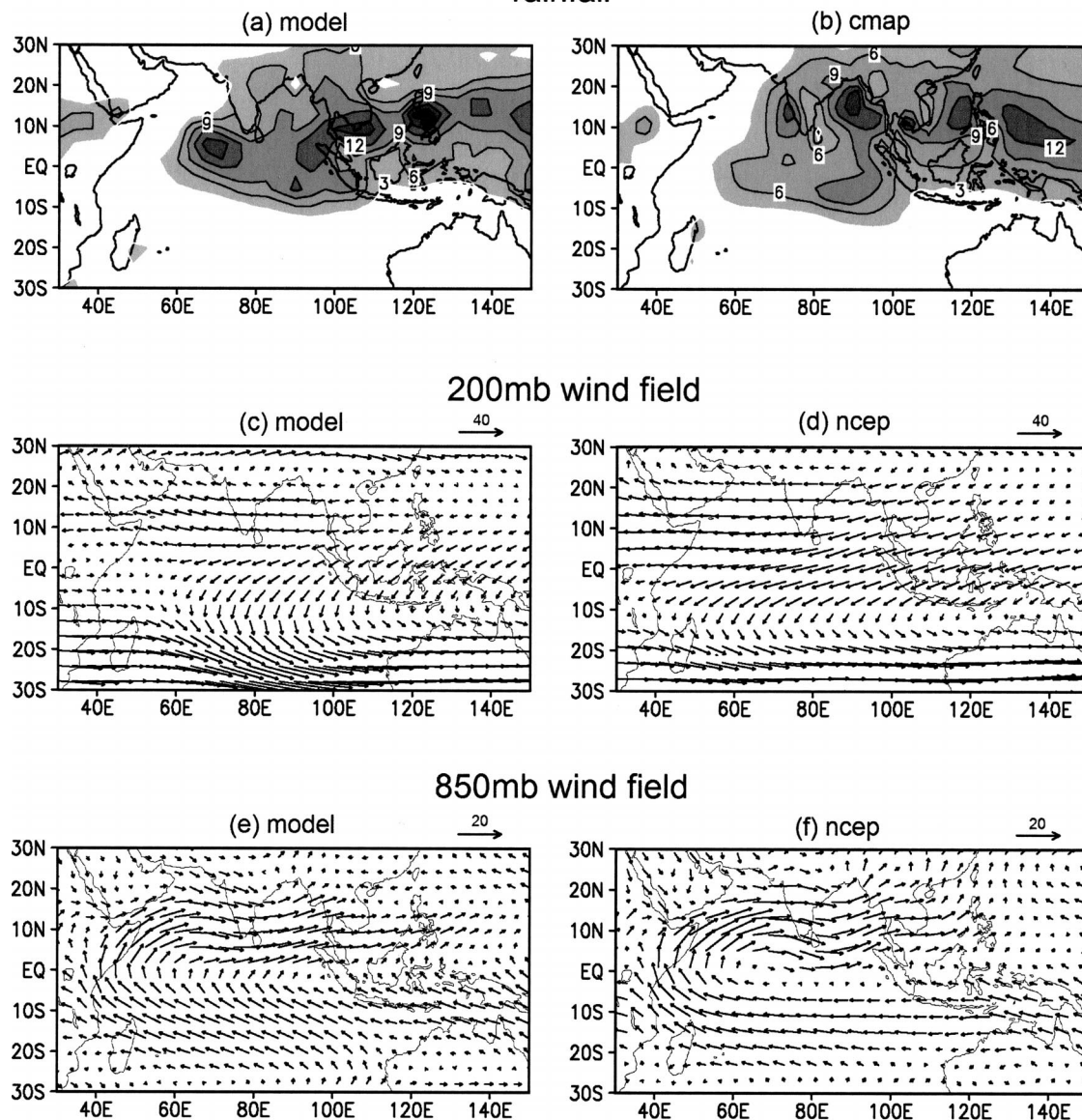
Summer (JJA) Mean State

rainfall

200mb wind field

850mb wind field

FIG. 1. The ECHAM simulated and observed summer mean (JJA) (a), (b) precipitation (mm day^{-1}); (c), (d) 200-mb wind; and (e), (f) 850-mb wind fields (m s^{-1}).

posite rainfall (base on the axis of the maximum rainfall) shown in Fig. 4. The average propagation speed from 0° to 20°N is about 1.0° day^{-1}, consistent with the observations. Note that the maximum rainfall center moves extremely slowly in the equatorial region, suggesting the different dynamic origin of the northward propagation near and off the equator.

Next, we apply the same analysis approach to the daily NCEP–NCAR reanalysis data. Here the negative OLR is used to represent the convection. Twenty-five strong northward propagation cases are selected. Figure 5 shows the composite evolution of the convection (neg-

ative OLR field), filtered with the intraseasonal period. The following BSISO features derived from the model are confirmed by the observational data. 1) A new convection is initiated over the western equatorial Indian Ocean and then moves to the eastern equatorial Indian Ocean along the equator. 2) After moving to the eastern equatorial Indian Ocean around 90°E, the convection begins to move northward toward the northern Bay of Bengal. 3) No clear evidence shows the connection between the northward propagation of the ISO convection over the Indian Ocean and the eastward propagation in the western equatorial Pacific Ocean.
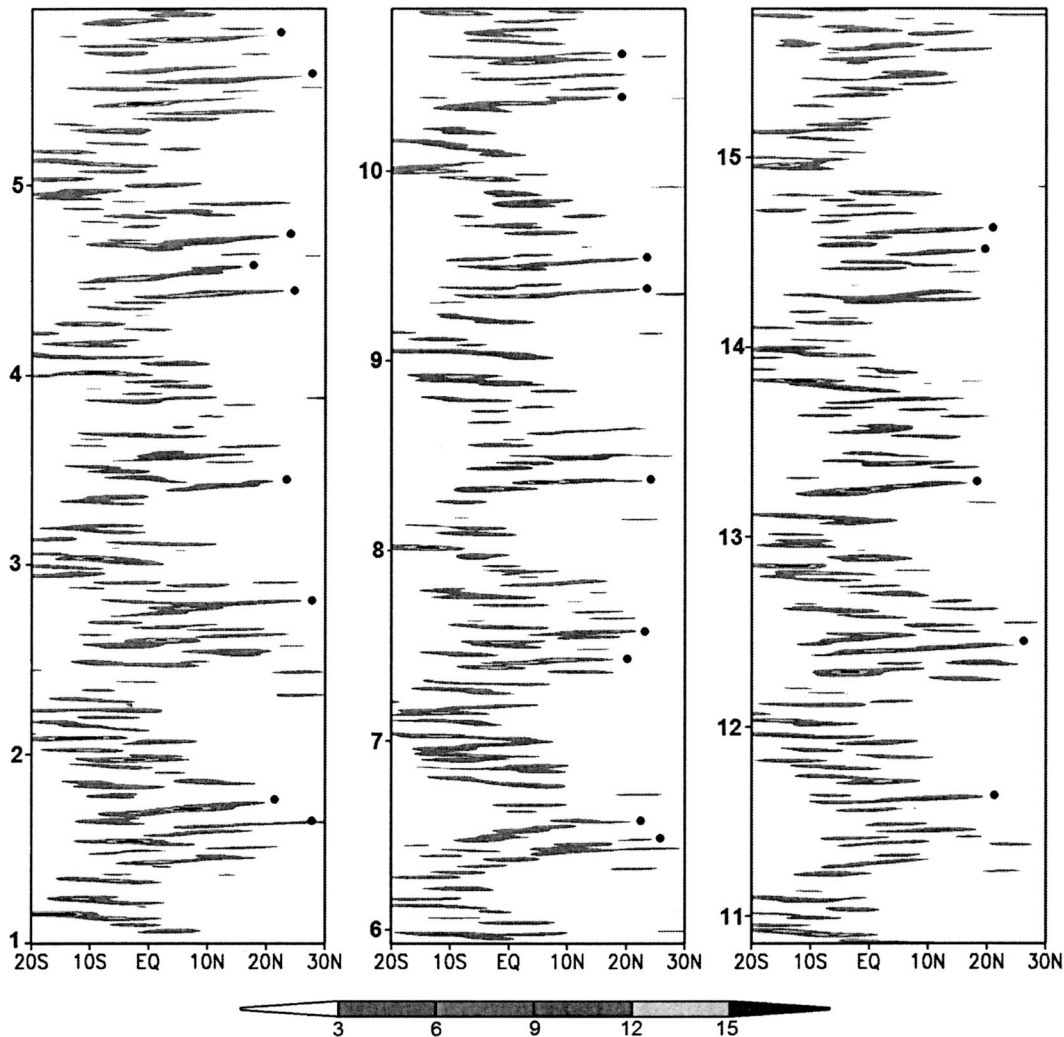
FIG. 2. Hovmöller diagram of the model ISO rainfall (mm day^{-1}) along 70°–95°E (only positive rainfall anomalies plotted). The vertical axis is time from model year 1 to 15. The solid dots denote the 23 strong northward propagation cases selected for composite analyses.

There is an important difference between the observed OLR and model precipitation composites. The observed OLR shows a northwest–southeast tilted band structure as it moves northward, which suggests the emanation of Rossby waves, whereas in the model rainbands are more or less zonal. The model simulation also shows less coherent movement of negative rainfall perturbations.

The meridional phase speed along 75°–90°E may be calculated based on the latitude–time profile of the observed OLR field (Fig. 6). The result shows that an average northward propagation speed is 0.93° latitude per day, similar to that obtained from the AGCM. The propagation speed is slower between 5°S and the equator and nearly constant from the equator to 25°N. Different from the model composite, the observed OLR composite exhibits a southward propagation with much weaker amplitude between 5°S and 15°S.

Next we examine the meridional phase relationship among various meteorological fields associated with the northward propagating BSISO mode in an attempt to unveil fundamental dynamics behind the northward propagation. Special attention is paid to the meridional asymmetry of dynamic and thermodynamic fields with respect to the convection center. The BSISO mode structure is composed based on the most significant northward propagation cases. We first construct the phase structure at each reference latitude over which the maximum convection occurs. As these phase structures bear great similarity, we further compose them with respect to the maximum convection center for different latitudes.

Figure 7 shows the meridional–vertical structure of the composite BSISO mode in the model. To clearly illustrate the meridional phase relationship, we have applied a cubic-spline interpolation for each field in the
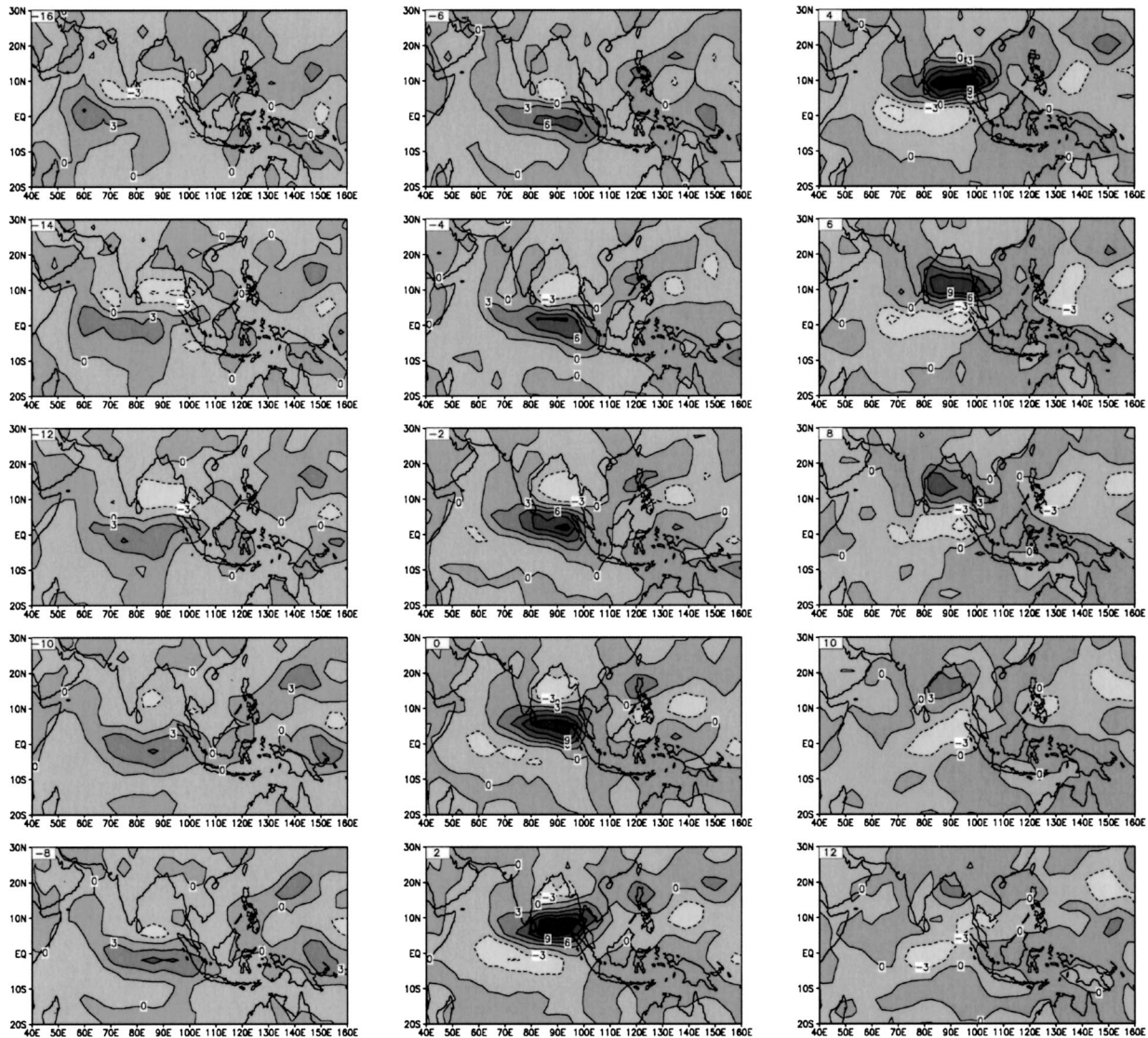
FIG. 3. Evolution of the model ISO rainfall composite (mm day^{-1}) from day -16 to day 12. Dark shading indicates the convection with positive rainfall perturbation and light shading indicates the suppressed convection with negative rainfall perturbation. Day 0 represents a reference time when the convection center moves to 5°N along 70°–95°E.

meridional direction. From Fig. 7, one can see that maximum vertical motion occurs in the middle troposphere (about 400 mb) and coincides with the convection center. Associated with this maximum ascending motion are the low-level convergence and the upper-tropospheric divergence.

The most striking asymmetric structure with respect to the convection center appears in the vorticity field. A positive vorticity center with an equivalent barotropic structure is located 400 km north of the convection center, while a negative vorticity with the same equivalent barotropic structure appears to the south of the convection center. Another striking asymmetry appears in the specific humidity field. A maximum specific humidity center shifts about 150 km to the north of the convection

center in the lower troposphere. The temperature and geopotential height fields also show a significant phase difference relative to the convection.

Figure 8 illustrates the observed counterparts of the BSISO structure. By comparison, one can find that most of the features simulated by the model, for instance, the northward shift of the equivalent barotropic vorticity and the low-level specific humidity, are well reflected by the NCEP–NCAR reanalysis. The resemblance of the model and observed BSISO structure and propagation characteristics suggests that to the first order of approximation, it is the internal atmospheric dynamics that are essential to cause the northward propagation. This is one of the motivations to conduct both observational and AGCM analyses.
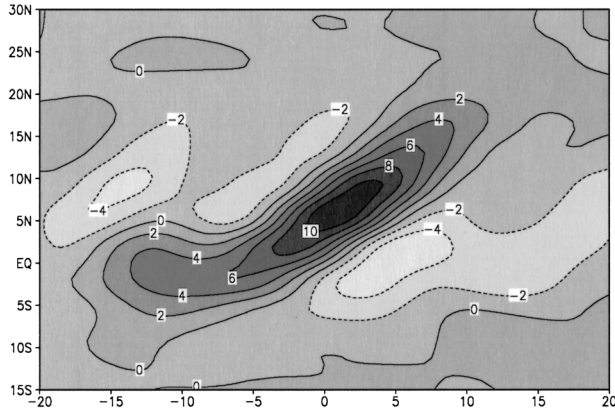
FIG. 4. Hovmöller diagram of the composite rainfall (mm day^{-1}) along 75°–90°E from the ECHAM model. Horizontal axis is time (day). The vertical axis is latitude.

A distinctive feature, compared to the model, lies in the low-level divergence and vertical velocity fields. In the NCEP–NCAR reanalysis data, the PBL convergence tends to lead the convection by 3°. This is accompanied by the tilting of the maximum vertical velocity axis. While the vertical motion at the middle–upper levels is in phase with the convection, it shifts to the north at the lower levels. It is likely that this northward shift of the PBL convergence results from the Ekman pumping induced by the positive vorticity at the top of the PBL ahead of the convection. The model, however, fails to capture this feature, possibly due to too strong turbulent mixing in the lower troposphere. This is partly reflected by the height of the maximum specific humidity center. While the observed maximum specific humidity center (Fig. 8e) is confined in the boundary layer below 850 mb, the model specific humidity peaks in a much higher attitude (around 650 mb).

4. Mechanisms for the northward propagation

In this section, based on meridional and vertical structures illustrated in the previous section, we intend to unveil the internal atmospheric dynamics responsible for the northward propagation of the BSISO.

a. The vertical shear mechanism

This mechanism is motivated by the observed and model BSISO structure that an equivalent barotropic vorticity field appears to the north of the convection center. In the following, by using a 2.5-layer intermediate atmospheric model, we demonstrate how the vertical shear of the summer mean flow leads to the coupling of barotropic and baroclinic modes and the development of a meridionally asymmetric barotropic vorticity field.

Figure 9 illustrates the vertical structure of the 2.5-layer model, following Wang and Li (1993, 1994). In

this model, there are a 2-layer free atmosphere and a well-mixed PBL. For simplicity we consider a 2D case with vanished zonal gradients for all variables. The governing equations for a linear motion on an f plane under a constant vertical shear of the mean zonal flow can be written as

$$\frac{\partial \zeta_-}{\partial t} + f_0 D_- = -\overline{u}_T \frac{\partial D_+}{\partial y} + K\nabla^2 \zeta_-, \tag{1}$$

$$\frac{\partial D_-}{\partial t} - f_0 \zeta_- + \nabla^2 \phi_- = K\nabla^2 D_-, \tag{2}$$

$$\frac{\partial \zeta_+}{\partial t} + f_0 D_+ = \overline{u}_T \frac{\partial}{\partial y}(2D_+ + D_-) + K\nabla^2 \zeta_+, \tag{3}$$

$$\frac{\partial D_+}{\partial t} - f_0 \zeta_+ + \nabla^2 \phi_+ = K\nabla^2 D_+, \tag{4}$$

$$\frac{\partial \phi_-}{\partial t} - f_0 \overline{u}_T v_+ + c_0^2(1 - I)D_- = c_0^2(B - 1)D_+$$
$$+ K\nabla^2 \phi_-, \tag{5}$$

where $\overline{u}_T = (\overline{u}_1 - \overline{u}_3)/2$ denotes the constant vertical shear of the mean flow and f_o is the Coriolis parameter at a reference latitude (12°N). Variables with a subscript, $+$ ($-$), represent a barotropic (baroclinic) mode. The detailed derivation of the governing equations is described in the appendix. Table 1 lists the description and standard values of major parameters in the equations. The use of an f plane is to exclude the Rossby wave emanation mechanism (Wang and Xie 1997; Lawrence and Webster 2002) so that one can focus on the effect of the basic-state vertical shear.

The motion in the PBL is controlled by the geopotential height at the top of the boundary layer, which is assumed to be equal to the geopotential height in the lower troposphere (Wang and Li 1993). Thus, we have

$$Eu_B - f_0 v_B = 0, \tag{6}$$

$$Ev_B + f_0 u_B = -\frac{\partial(\phi_+ - \phi_-)}{\partial y}. \tag{7}$$

Equations (6), (7) lead to

$$\frac{-E}{E^2 + f_0^2} \frac{\partial^2(\phi_+ - \phi_-)}{\partial y^2} = \frac{\partial v_B}{\partial y} = \frac{w_B}{p_s - p_e}$$
$$= -\frac{2\Delta p}{p_s - p_e}D_+, \tag{8}$$

where E is the Ekman coefficient.

Consider a simple case in which we have convection with a purely baroclinic structure, that is, initially the barotropic mode is zero. Based on Eq. (3), the generation of the barotropic mode in the free atmosphere can only be realized through the vertical shear of the mean flow acting on the meridional gradient of the baroclinic divergence; that is,
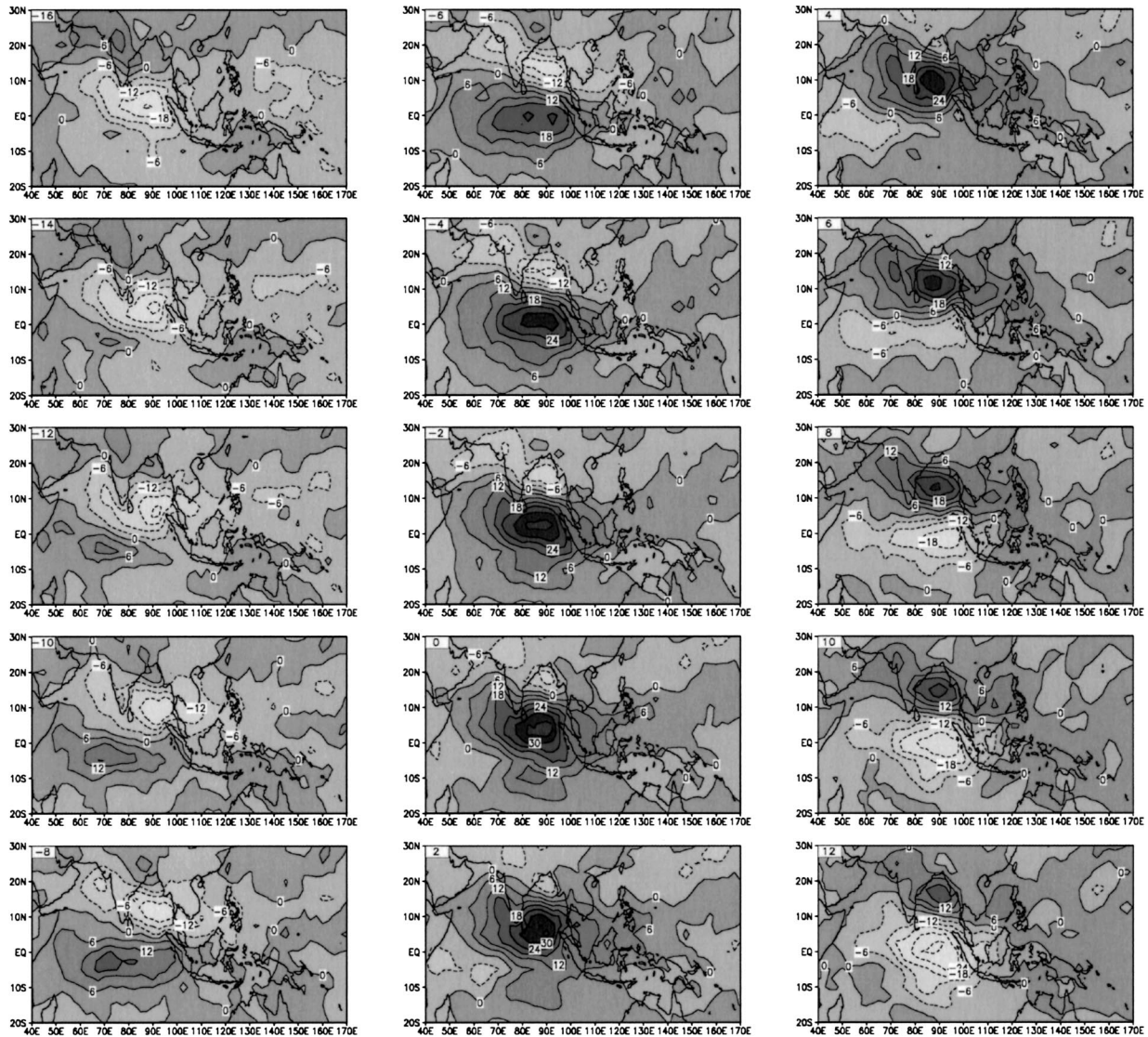
FIG. 5. As in Fig. 3 except for the negative OLR (W m^{-2}) evolution from the NCEP–NCAR reanalysis. Dark shading indicates the convection with negative OLR perturbation. Light shading indicates the suppressed convection with positive OLR perturbation.
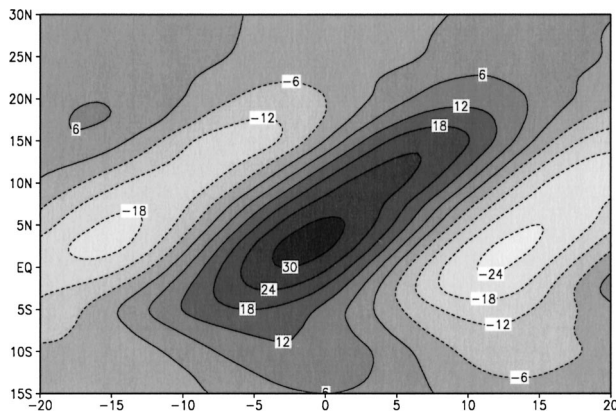

FIG. 6. As in Fig. 4 except for the composite negative OLR (W m^{-2}) from the NCEP–NCAR reanalysis.

$$\frac{\partial \zeta_+}{\partial t} \propto \overline{u}_T \frac{\partial D_-}{\partial y}. \tag{9}$$

The generation of the barotropic vorticity may further lead to the development of the barotropic divergence in the free atmosphere:

$$\frac{\partial D_+}{\partial t} \propto f_0 \zeta_+. \tag{10}$$

Equation (9) implies that the baroclinic and barotropic modes are closely coupled in the presence of the vertical shear of the mean flow. In reality, the vertical structure of the atmospheric mean flow in boreal summer is characterized by a strong easterly shear in the monsoon region.

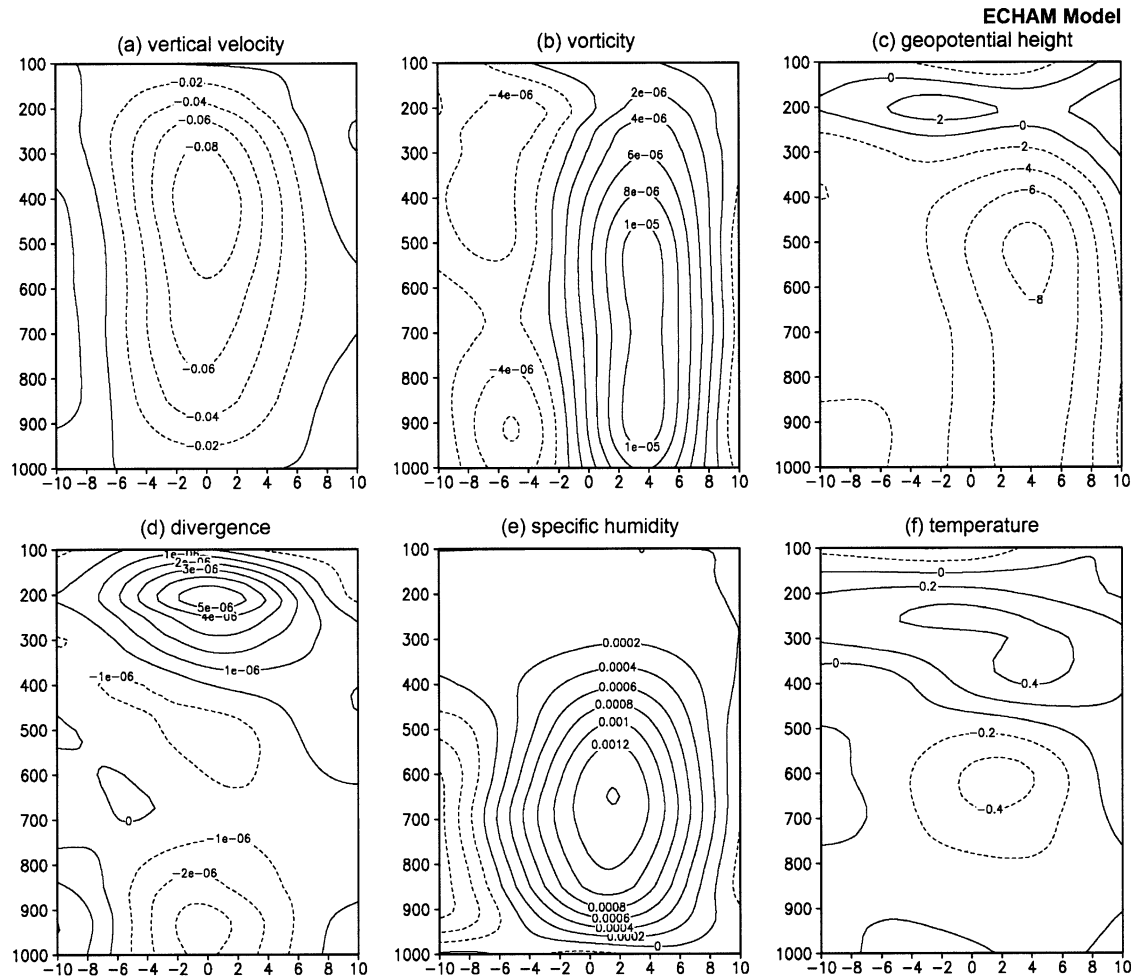Figure 10 is a schematic diagram illustrating how the

ECHAM Model

(a) vertical velocity   (b) vorticity   (c) geopotential height

(d) divergence   (e) specific humidity   (f) temperature

FIG. 7. Meridional–vertical structures of the northward propagating BSISO mode derived from the ECHAM model: (a) vertical velocity (hPa s^{-1}), (b) vorticity (s^{-1}), (c) geopotential height (dam), (d) divergence (s^{-1}), (e) specific humidity (kg kg^{-1}), and (f) temperature (K). Horizontal axis is the meridional distance (°lat) with respect to the convection center. The positive (negative) value means to the north (south) of convection center. The vertical axis is the pressure (hPa).

easterly shear leads to the northward propagation of the BSISO convection. In response to the convective heating in the middle troposphere, a convergence (divergence) occurs in the lower (upper) troposphere with maximum vertical motion appearing in the mid troposphere (Fig. 10a). Therefore, a maximum positive baroclinic divergence coincides with the convection center, and $\partial D_-/\partial y < 0$ ($\partial D_-/\partial y > 0$) north (south) of the convection center (Fig. 10b). Consider the easterly shear of the mean flow in the summer Asian monsoon region (Fig. 10c), based on Eq. (9), a positive barotropic mode of vorticity will be induced to the north of the convection and a negative vorticity to the south (Figs. 10d,e).

The positive barotropic vorticity ahead of the convection may induce a barotropic divergence in situ in the Northern Hemisphere [$f_0 > 0$, according to Eq. (10)]. The free-atmosphere divergence leads further to a boundary layer convergence in order to satisfy the continuity equation (Fig. 10f). The boundary layer mois-

ture convergence favors the development of convective heating to the north of the previous convection center, and as a result, the convection moves northward.

The phase leading of the PBL convergence to the convection is clearly seen from the structure derived from the reanalysis data, but less clearly from the AGCM output. However, both data clearly show phase leading in the sea level pressure and lower-tropospheric geopotential height. This is because the consequence of the free-atmosphere divergence leads to not only the convergence in the PBL (to partially compensate the loss of the mass), but also the drop of the surface pressure. It is the generation of negative geopotential height in front of the convection that gives rise to the tendency of a northward shift of the convergence in the lower troposphere. This is clearly seen from our analysis of the model low-level divergence budget (figure not shown).

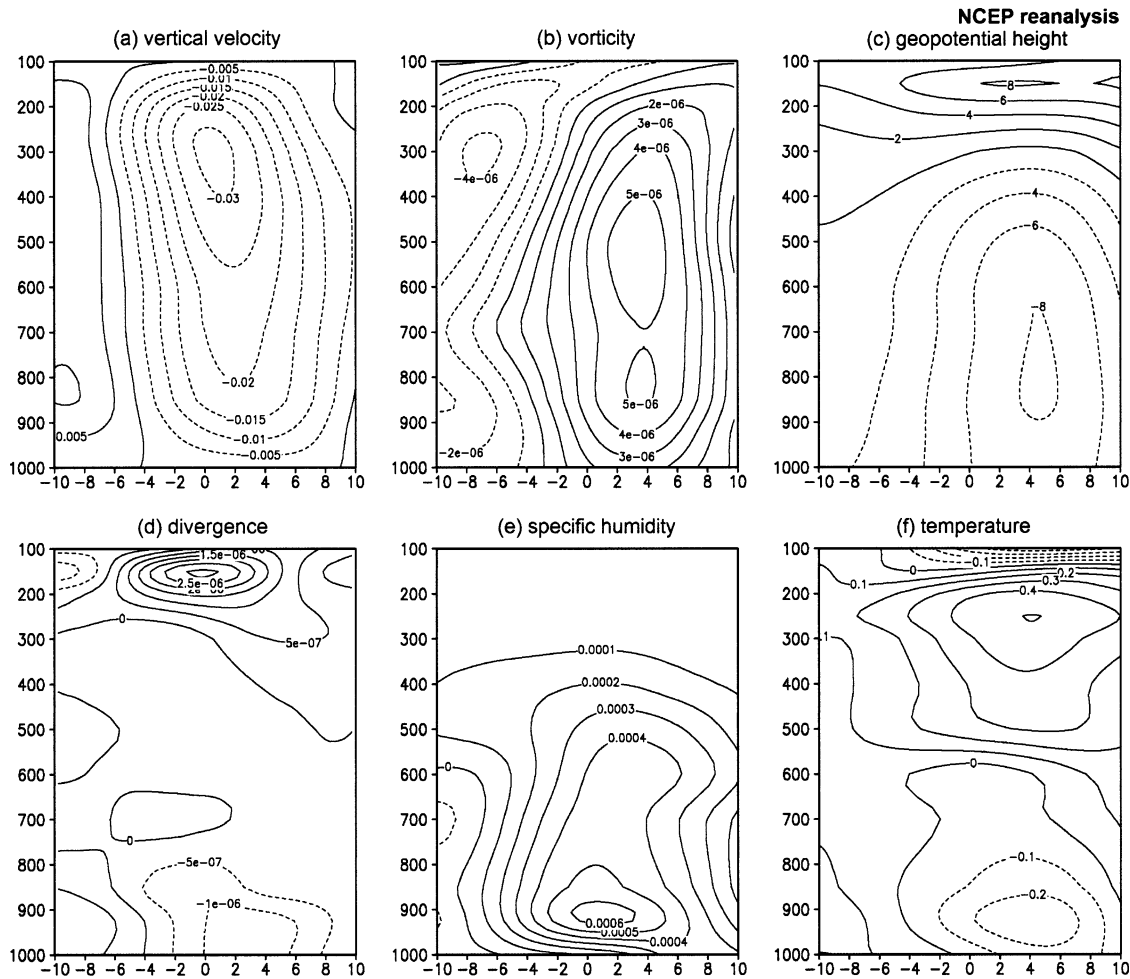To summarize, the prevailing easterly shear over the

FIG. 8. As in Fig. 7 except for the NCEP–NCAR reanalysis.

South Asian monsoon region may cause the generation of the barotropic vorticity to the north of a convection, leading to the northward shift of both the moisture convergence in the PBL and the negative geopotential height in the lower troposphere and thus the northward propagation of the convection.
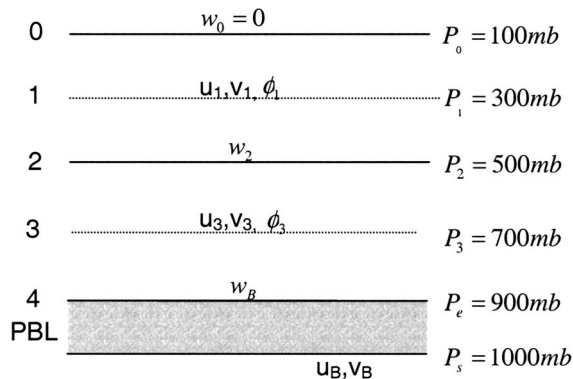

FIG. 9. Vertical structure of the 2½-layer model (Wang and Li 1993).

It is worth noting that the vertical shear mechanism mentioned above is only valid away from the equator in the Northern Hemisphere (say, north of 5°N). This is because in the equatorial region the Coriolis parameter is extremely small, and the negative sign of the Coriolis parameter implies the southward propagation in the presence of the easterly shear. However, in both model and reality, the northward propagation starts from around 5°S. This points out that other physical mechanisms, in addition to the vertical shear, must act to contribute to the northward propagation. This leads to our discussion in next subsection of the moisture–convection feedback.

b. Moisture–convection feedback mechanism

The BSISO structures analyzed from both the AGCM and reanalysis data show a clear phase leading of the specific humidity to the convection. It is argued that this meridional asymmetry may cause the northward shift of the convective heating, leading to the northward movement of the convection. A key question is what

TABLE 1. Parameters and their standard values in the simple dynamic framework.

b	Precipitation efficiency coefficient	0.8
C_d	Surface heat exchange coefficient	1.5×10^{-3}
C_p	Specific heat at a constant pressure	1004 J K^{-1} kg^{-1}
K_q	Evaporation coefficient	6.95×10^{-4}
$-\boldsymbol{\nabla} \cdot \overline{\mathbf{V}}$	Convergence of the mean flow	3×10^{-6} s^{-1}
f_0	Coriolis parameter	f (12°N)
C_0	Gravity wave speed of the first baroclinic mode	50 m s^{-1}
$\overline{u}_T$	Vertical shear of the mean zonal flow	-12 m s^{-1}
I	Heating coefficient associated with wave convergence	0.85
B	Heating coefficient associated with frictional convergence	1.95
E	Ekman coefficient	0.18×10^{-5} s^{-1}
K	Meridional diffusion coefficient	6×10^{4} m^2 s^{-1}
P_s	Pressure at the bottom of the model	1000 mb
P_e	Pressure at the top of the boundary layer	900 mb
P_2	Pressure at level 2 of the model	500 mb
dp	Depth between 2 model levels in the free atmosphere	400 mb
$\overline{u}_B$	Zonal mean flow in the PBL	4 m s^{-1}
$\overline{v}_B$	Meridional component of the mean flow in the PBL	3 m s^{-1}
$\|\overline{V}_m\|$	Wind speed of the mean flow in PBL ($=\sqrt{\overline{u}_B^2 + \overline{v}_B^2}$)	5 m s^{-1}
α_1	Heating coefficient associated with surface evaporation	3.7×10^{-4} m^2 K^{-1} s^{-3}
α_2	Heating coefficient associated with moisture perturbation in PBL	0.17 m^2 s^{-3}
λ	Coefficient associated with the wind–evaporation feedback	1.2×10^{-8}

causes the asymmetric distribution of the specific humidity. In the following we propose two possible mechanisms.

1) MOISTURE ADVECTION BY THE MEAN FLOW

The observed summer mean flow over the eastern Indian Ocean sector shows a prevailing northward component in the PBL (Fig. 11). It is hypothesized that the moisture advection by this northward summer mean flow in the boundary layer together with the advection of the mean specific humidity by the perturbation vertical motion in the PBL may be, at least partially, responsible for the asymmetry of the specific humidity with respect to the convection.

Mathematically, this mechanism may be expressed as

$$\frac{\partial q}{\partial t} \propto -\overline{v}_B \frac{\partial q}{\partial y} - w_B \frac{\partial \overline{q}}{\partial p}.$$

Physically, it is interpreted as follows (see the schematic diagram in Fig. 12). Consider a strong ISO convection with convergence at the surface level and divergence at the upper level. The convergence at the surface level will induce the upward motion in the atmospheric boundary layer, which will bring the rich moisture at the surface to a certain level in the PBL (Fig. 12a). The advection effect by the summer mean meridional wind in the PBL may further shift the specific humidity center to the north of the convection (Fig. 12b). As the convective heating largely depends on the moisture convergence, the shifted moisture center will lead to the northward displacement of the convective heating and thus the convection tends to move northward (Fig. 12c).

2) MOISTURE ADVECTION DUE TO THE MEAN MERIDIONAL MOISTURE GRADIENT

Another possible mechanism that leads to the northward shift of the moisture is through the advection effect by the ISO wind in the presence of the mean meridional specific humidity gradient. Figure 13 shows the meridional distribution of the summer mean [June–August (JJA)] specific humidity at the surface averaged over the Indian subcontinent sector. During the summer monsoon season the maximum moisture is located around 20°N over the northern Indian Ocean. To the south of 20°N, the meridional gradient of the mean specific humidity is positive. Considering the advection by the ISO wind, the moisture equation may be written as

$$\frac{\partial q}{\partial t} \propto -v_B \frac{\partial \overline{q}}{\partial y}.$$

In response to the ISO convective heating, the perturbation wind has a southward flow to the north and a northward flow to the south of the convection center. As a result, the moist perturbation has an asymmetric structure with a positive center appearing to the north of the convection center and a negative center to the south of the convection (Fig. 14).

This second moisture advection mechanism has, in fact, already incorporated in Li and Wang's (1994) modeling results. In that study Li and Wang used an intermediate atmospheric model without the effect of the summer mean flow. A climatological July mean SST field is specified that has a maximum SST at 20°N over the northern Indian Ocean. The surface moisture in the model is completely controlled by the mean SST based on an empirical relationship. The model simulations indicate that the asymmetric mean thermal condition with respect to the equator leads to a
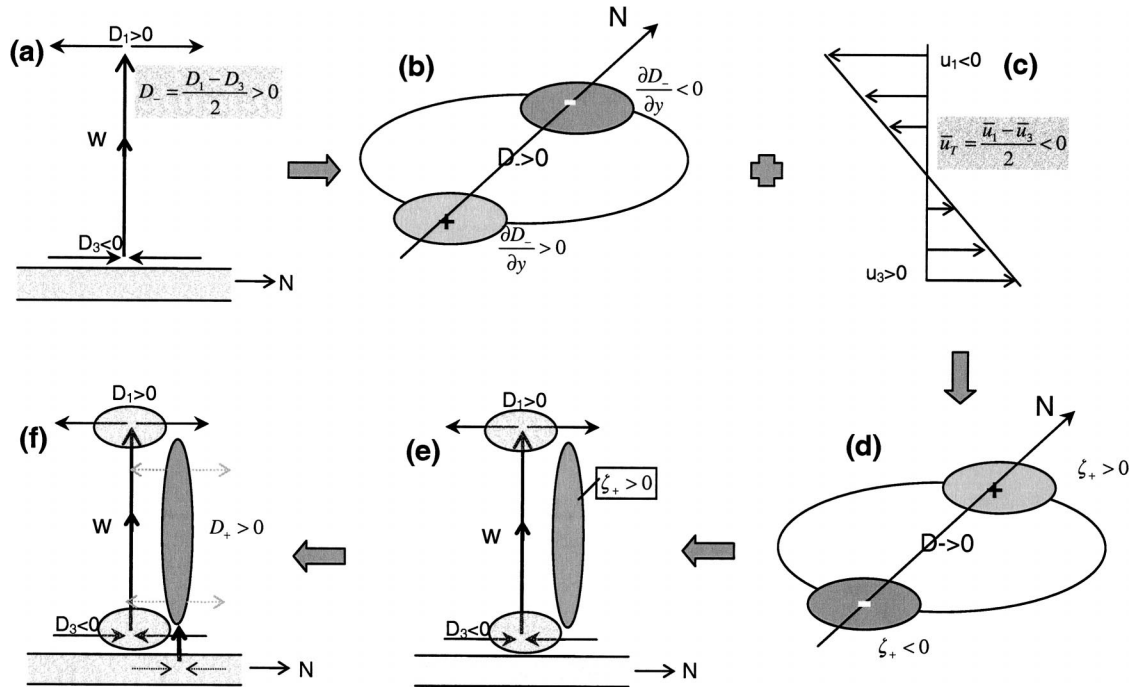
FIG. 10. Schematic diagram for the vertical shear mechanism. (a) Consider initially an ISO convection with a baroclinic structure. (b) This leads $\partial D_-/\partial y < 0$ ($\partial D_-/\partial y > 0$) north (south) of the convection center. (c) In the presence of the easterly shear of the mean flow, (d), (e) a positive barotropic vorticity is induced north of the convection, leading to (f) a barotropic divergence in situ. The latter further leads to a PBL convergence and thus a northward shift of convective heating.

northward propagation over the Indian and western Pacific Ocean sectors. This moisture–convection feedback mechanism works for all latitudes from 10°S to 20°N (including the equatorial region), providing a valuable addition to the vertical shear mechanism for explaining the observed northward propagation feature.

5. Eigenvalue analysis

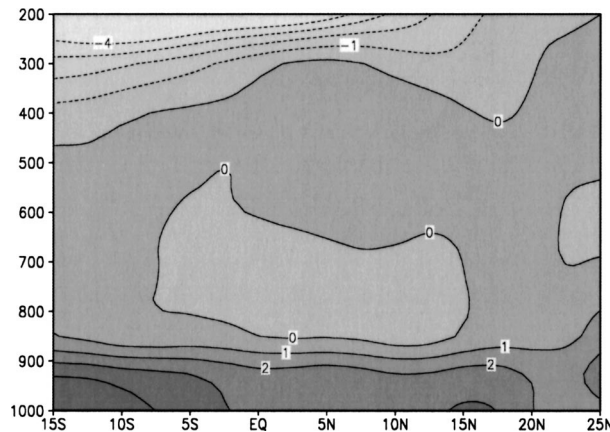Why is the northward propagation pronounced during the boreal summer in the monsoon region? Is the

FIG. 11. Meridional–vertical profile of the north–south component of the summer mean flow (m s^{-1}) averaged between 70° and 95°E.

northward propagating BSISO an unstable mode of the summer mean flow? What is the relative role of the vertical shear versus moisture–convection feedback and internal dynamics versus air–sea interaction in causing the northward propagation? In this section we intend to answer these questions using a unified theoretical framework.

The dynamic framwork used for an eigenvalue analysis is based on Wang and Li (1993) 2½-layer atmospheric model [see Eqs. (1)–(8)] coupled to a simple constant mixed layer ocean model. A modification has been made in the thermodynamics equation to include the convective heating associated with the SST effect and the perturbation moisture convergence in the PBL. Thus, the thermodynamic equation can be rewritten as

$$\frac{\partial \phi_-}{\partial t} - f_0 \bar{u}_T v_+ + c_0^2 (1 - I) D_-$$

$$= c_0^2 (B - 1) D_+ + \alpha_1 T + \alpha_2 q + K \nabla^2 \phi_-, \quad (11)$$

where α_1, α_2 are the heating coefficients expressed as

$$\alpha_1 = bRgL_c \rho C_d |\bar{V}_m| K_q/(2C_p P_2),$$

$$\alpha_2 = bRgL_c (P_s - P_e)(-\nabla \cdot \bar{V})/(2C_p P_2).$$

The eigenvalue system is closed after introducing the perturbation moisture and SST equations, which are
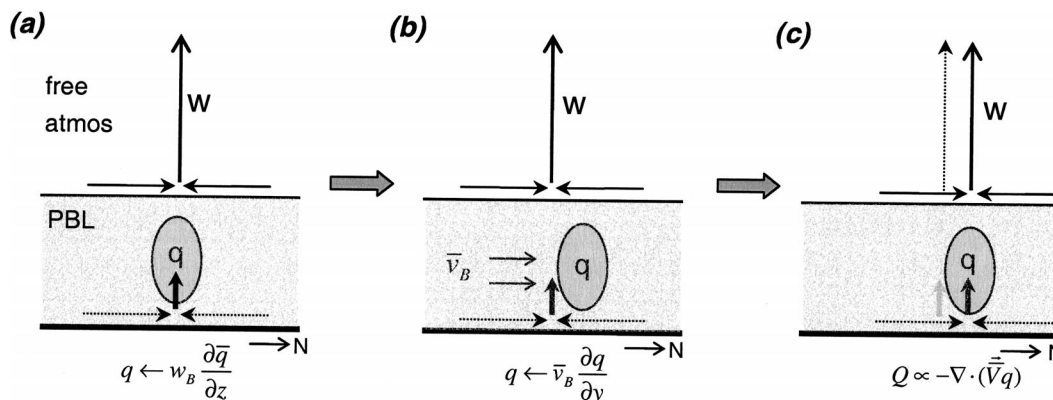
FIG. 12. Schematic diagram for the mechanism of moisture advection by mean flow. (a) The specific humidity perturbation caused by Ekman pumping is advected (b) by the mean northward meridional wind in the PBL, (c) which leads to the northward shift of moisture convergence and thus convective heating to the convection center.

$$\frac{\partial q}{\partial t} = -v_B \frac{\partial \overline{q}}{\partial y} - \overline{v}_B \frac{\partial q}{\partial y} - w_B \frac{\partial \overline{q}}{\partial p} + K \nabla^2 q, \quad (12)$$

$$\frac{\partial T}{\partial t} = -\lambda \overline{u}_B u_B + K \nabla^2 T. \quad (13)$$

Note that in the SST equation above, we consider only the wind–evaporation–SST feedback (Wang and Li 1994; Xie and Philander 1994; Li 1997) and horizontal diffusion.

Equations (1)–(4) and (11)–(13), together with the boundary layer constraints Eqs. (6)–(8) form a complete dynamic system for an eigenvalue analysis. Table 1 lists the standard values of major parameters.

First, we consider the simplest case in which the effect of the perturbation moisture and SST is neglected. An analytical solution for the growth rate and frequency is readily derived, if one assumes that the divergence tendency vanishes (i.e., $\partial D_+/\partial t = 0$ and $\partial D_-/\partial t = 0$). For a 2D ($y$–$z$ plane) system, this assumption is equivalent to a long-wave approximation (i.e., the local time change rate of the meridional wind component van-
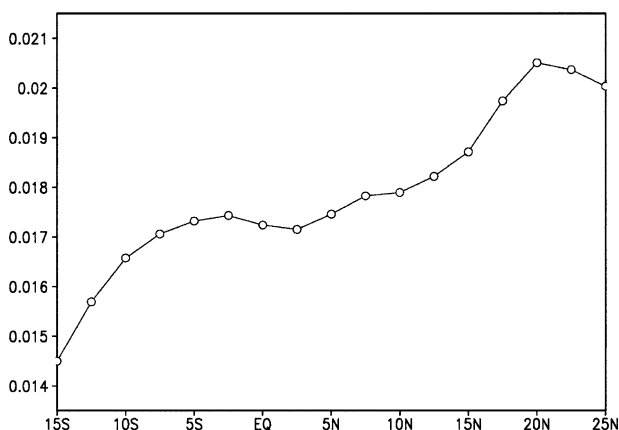

FIG. 13. Meridional profile of the summer mean specific humidity (kg kg^{-1}) at 1000 mb averaged between 70° and 95°E.

ishes). To validate this assumption, the eigenvalue problems are solved with and without $\partial D_+/\partial t$ and $\partial D_-/\partial t$ terms, and solutions are very close.

The divergence, vorticity, and meridional wind component may be represented as a function of velocity potential (χ) and streamfunction (ψ):

$$D_+ = \nabla^2 \chi_+, \qquad \zeta_+ = \nabla^2 \psi_+, \qquad D_- = \nabla^2 \chi_-,$$

$$\zeta_- = \nabla^2 \psi_-, \qquad v_+ = \frac{\partial \chi_+}{\partial y}.$$

Consider a finite domain (10^7 m) with a periodic meridional boundary condition and a wave solution of $e^{i(ly - \sigma t)}$. The governing equations may be written as

$$\frac{\partial \psi_-}{\partial t} + f_o \chi_- = -\overline{u}_T \frac{\partial \chi_+}{\partial y} + K \nabla^2 \psi_-, \quad (14)$$

$$-f_o \psi_- + \phi_- = 0, \quad (15)$$

$$\frac{\partial \psi_+}{\partial t} + f_o \chi_+ = 2\overline{u}_T \frac{\partial \chi_+}{\partial y} + \overline{u}_T \frac{\partial \chi_-}{\partial y} + K \nabla^2 \psi_+, \quad (16)$$

$$-f_o \psi_+ + \phi_+ = 0, \quad (17)$$

$$\frac{\partial \phi_-}{\partial t} - f_o \overline{u}_T \frac{\partial \chi_+}{\partial y} + c_0^2 (1 - I)(-l^2 \chi_-)$$
$$= c_0^2 (B - 1)(-l^2 \chi_+) + K \nabla^2 \phi_-, \quad (18)$$

$$\psi_+ - \psi_- = \frac{A}{f_o} \chi_+, \quad (19)$$

where $A = [(E^2 + f_0^2)/E] \, 2dp/(P_s - P_e)$.

Thus, a single equation for the barotropic velocity potential may be derived, which is

$$\frac{\partial \chi_+}{\partial t} = -\frac{f_0^2}{A} \left[1 + \frac{c_0^2 (B - 1)(-l^2)}{f_0^2 + c_0^2 (1 - I) l^2} \right] \chi_+$$
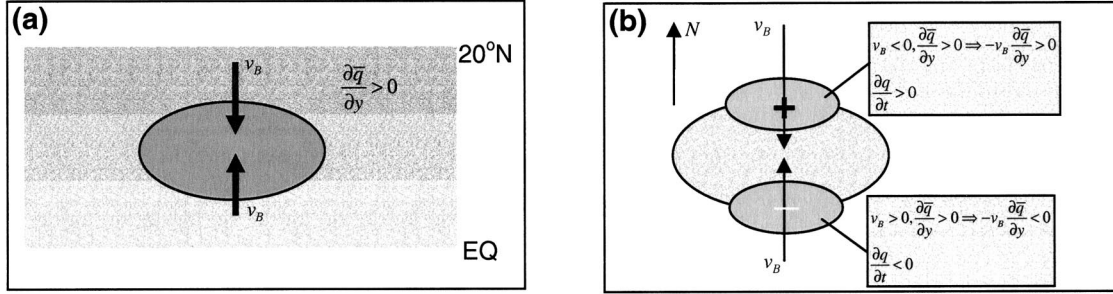
FIG. 14. Schematic diagram for the mechanism of moisture advection by the ISO wind in the presence of the mean specific humidity gradient. The meridional asymmetric mean specific humidity field is advected by convection-induced perturbation wind, (a) southward to the north of a convection center and northward to the south, which leads to a (b) positive moisture perturbation to the north and negative to the south of the convection center. As a result, the convection tends to move northward.
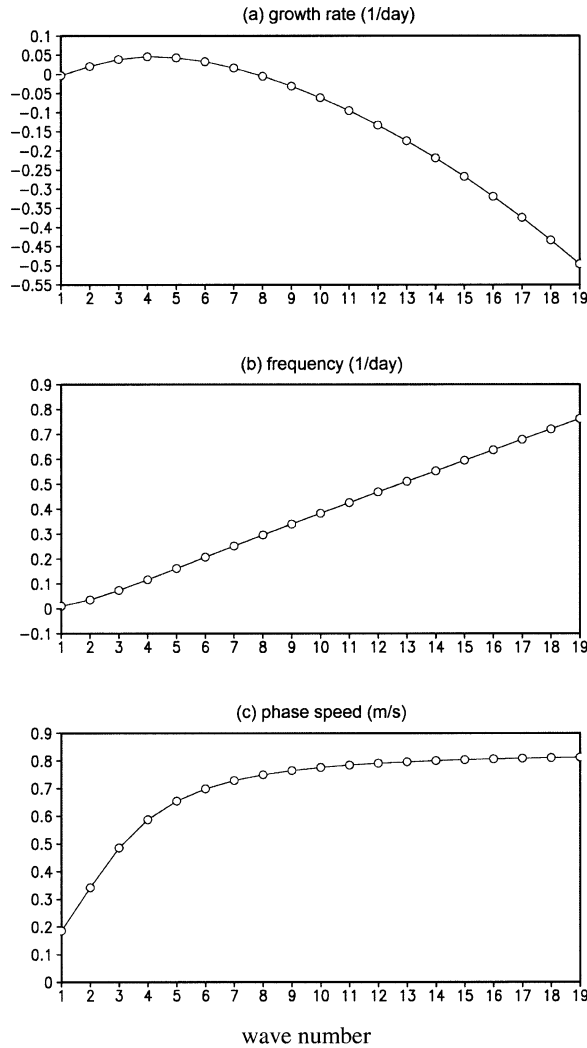

FIG. 15. Eigenvalue solutions for (a) growth rate (day^{-1}) and (b) frequency (day^{-1}) and phase speed (m s^{-1}) as a function of wavenumber.

$$+ \frac{\overline{u}_T f_0}{A}\left[2 + \frac{c_0^2(B-1)l^2}{f_0^2 + c_0^2(1-I)l^2}\right.$$

$$\left. + \frac{c_0^2(1-I)l^2 - f_0^2}{f_0^2 + c_0^2(1-I)l^2}\right]\frac{\partial \chi_+}{\partial y}$$

$$- \frac{2\overline{u}_T^2 f_0^2}{A[f_0^2 + c_0^2(1-I)l^2]}\frac{\partial^2 \chi_+}{\partial y^2} + K\nabla^2\chi_+. \tag{20}$$

Let $\sigma = \sigma_r + i\sigma_i$, we obtain an analytical solution for the growth rate and frequency:

$$\sigma_i = -\frac{f_0^2}{A}\left[1 + \frac{c_0^2(B-1)(-l^2)}{f_0^2 + c_0^2(1-I)l^2}\right]$$

$$+ \frac{2\overline{u}_T^2 f_0^2 l^2}{A[c_0^2(1-I)l^2 + f_0^2]} - Kl^2, \tag{21}$$

$$\sigma_r = -\frac{\overline{u}_T f_0 l}{A}\left[2 + \frac{c_0^2(B-1)l^2}{f_0^2 + c_0^2(1-I)l^2}\right.$$

$$\left. + \frac{c_0^2(1-I)l^2 - f_0^2}{f_0^2 + c_0^2(1-I)l^2}\right]. \tag{22}$$

The solution above shows that the growth rate is proportional to the second power of the vertical shear, while the frequency is proportional to the first power of the vertical shear. Thus the meridional phase speed depends on the vertical shear. For the easterly shear case ($\overline{u}_T < 0$), the BSISO mode always propagates northward in the Northern Hemisphere.

The dependence of the growth rate and frequency on meridional wavenumber is illustrated in Fig. 15. The BSISO mode is most unstable at wavenumber 4, which corresponds to a wavelength of 2500 km. The growth rate for this most unstable mode is in the intraseasonal range (with regard to its e-folding time scale). For an easterly shear of -12 m s^{-1}, the corresponding meridional phase speed is about 0.6 m s^{-1}. All these values are within a reasonable range of the observed values.

Figure 16 shows the relationship between the phase speed and growth rate of the most unstable mode and the vertical shear intensity. The phase speed is linearly proportional to the vertical shear. With a zero vertical shear, there would be no northward propagation. With the increase of the easterly shear intensity, say, from

-12 to -24 m s^{-1}, the northward phase speed increases from 0.6 to 1.2 m s^{-1}. The growth rate increases parabolically with the square of the vertical shear intensity.

Next, we examine the effect of the air–sea interaction and the moisture–convection feedback. The barotropic velocity potential equation may be written as

$$\frac{\partial \chi_+}{\partial t} = -\frac{f_0^2}{A}\left[1 + \frac{c_0^2(B-1)(-l^2)}{f_0^2 + c_0^2(1-I)l^2}\right]\chi_+ + \frac{\overline{u}_T f_0}{A}\left[2 + \frac{c_0^2(B-1)l^2}{f_0^2 + c_0^2(1-I)l^2} + \frac{c_0^2(1-I)l^2 - f_0^2}{f_0^2 + c_0^2(1-I)l^2}\right]\frac{\partial \chi_+}{\partial y}$$

$$- \frac{2\overline{u}_T^2 f_0^2}{A[f_0^2 + c_0^2(1-I)l^2]}\frac{\partial^2 \chi_+}{\partial y^2} - \frac{f_0}{A[f_0^2 + c_0^2(1-I)l^2]}\left[\overline{u}_T \alpha_1 \frac{\partial T}{\partial y} + \overline{u}_T \alpha_2 \frac{\partial q}{\partial y} + f_0 \alpha_1 T + f_0 \alpha_2 q\right] + K\nabla^2 \chi_+. \quad (23)$$

Equation (23), together with Eqs. (12)–(13), forms a closed eigenvalue system. The effect of individual processes on the northward propagation may be revealed by simply switching off some model parameters. For instance, by setting $\overline{u}_T$, α_1, or α_2 to be zero, one may exclude the effect of the vertical shear, the SST feedback, and the moisture feedback, respectively. Table 2 shows the results in the presence of each of the aforementioned processes. While the sole effect of the vertical shear contributes to a northward phase speed of about 0.6 m s^{-1}, the effects of moisture advection by the mean flow or by the mean meridional moisture gradient and the air–sea interaction contribute approximately equally to a northward phase speed of 0.2 m s^{-1}. Due to a difference in the most unstable wavelength, the total northward phase speed is slightly different from the sum of individual speeds, both of which are in a realistic range. Since the simple dynamic framework contains various assumptions such as the omission of ocean mixing effects on SST and mean flow advection in the PBL momentum equations, the comparison between the contributions of different processes is qualitative rather than quantitative.

6. Summary and discussion

In this study, the spatial and temporal structure of the northward propagating BSISO mode is revealed based on the analysis from the ECHAM simulation and the NCEP–NCAR reanalysis. The comparison of the AGCM output with the NCEP–NCAR reanalysis shows that the evolution features of the BSISO simulated by the ECHAM AGCM bears close similarities with those derived from the reanalysis data.

Our composite analysis reveals that after being initiated in the western equatorial Indian Ocean, the convection associated with the BSISO mode propagates eastward along the equator. Over the eastern equatorial Indian Ocean around 90°E, the convection begins to move northward to the northern Indian Ocean. Both the AGCM simulation and the NCEP–NCAR reanalysis

show a northward phase speed of about 1 m s^{-1} between 5° and 20°N and a slower phase speed near and south of the equator. The composite analysis mainly captures the independent northward propagation events, as there is no obvious connection between the northward propagation in the Indian Ocean and the eastward propagation in the equatorial western Pacific.

The diagnosis of the northward propagating BSISO mode structure unveils that there are significant meridional asymmetries, with respect to the convection center, in the vorticity and moisture fields. A positive vorticity center with an equivalent barotropic structure is located a few degrees north of the convection center. The perturbation specific humidity, which has a maximum center in the lower troposphere, also tends to lead the convection by a couple of degrees.

A simple theoretical model is advanced to understand the origin of the northward propagation. Based on the BSISO structure, we propose two internal atmospheric dynamics mechanisms:

1) *The vertical shear mechanism.* The summer mean flow in the monsoon region is characterized by a strong easterly shear. This vertical shear couples the baroclinic and barotropic modes in the free atmosphere and leads to the generation of barotropic vorticity and divergence to the north of the convection. The latter further leads to the northward shift of the moisture convergence in the PBL and thus the ISO convection. However, this mechanism is effective only away from the equator in the Northern Hemisphere.

2) *The moisture–convection feedback mechanism.* Two processes contribute to the northward shift of the specific humidity in the lower troposphere. They are 1) the moisture advection by the mean southerly in the PBL and 2) the advection of the mean specific humidity gradient by the perturbation wind. The asymmetric moisture distribution further leads to the northward shift of the convective heating and as a result the BSISO mode moves northward.

TABLE 2. Contribution of the northward propagation speed by different mechanisms.

Mechanisms	Phase speed (m s^{-1})
Vertical shear	0.6
Moisture advection by mean flow in PBL $\left(\overline{v}_B \frac{\partial q}{\partial y} + w_B \frac{\partial \overline{q}}{\partial p} \right)$	0.2
Moisture advection by anomalous flow $\left(v_B \frac{\partial \overline{q}}{\partial y} \right)$	0.2
Air–sea interaction	0.2
Total	0.9

Our eigenvalue analysis indicates that the northward propagating BSISO mode is an unstable mode of the summer mean flow in the monsoon region. This explains the frequent appearance of the northward propagation of the BSISO convection in the region. The analysis result also points out the relative importance of various processes in contributing to the northward propagation. While the vertical shear plays an important role away from the equator in the Northern Hemisphere, the moisture–convection feedback and air–sea interaction also contribute significantly, particularly in the region near and south of the equator. Overall, given the similar structure and propagation characteristics of the BSISO in the model and the observation, we conclude that it is the internal atmospheric dynamics that are essential to give rise to the northward propagation over the tropical Indian Ocean.

A discrepancy of the model compared to the observed BSISO structure is the phase of the low-level convergence. With the NCEP–NCAR reanalysis data, the low-level convergence appears to lead the convection by 2–3° with the vertical motion axis tilting to the north at the lower level. It is likely that this northward shift is caused by the Ekman pumping due to the positive vorticity forcing at top of the PBL. However, this shift does not appear in the model, pointing out the need for improvement of the PBL dynamics in the ECHAM.
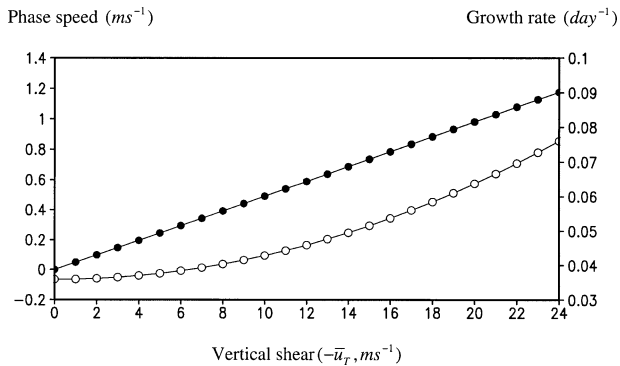
Our observational and AGCM analyses indicate that strong northward propagating BSISOs do not depend on the equatorial eastward moving component. Thus, the mechanisms proposed here are fundamentally different from the Rossby wave emanation mechanism proposed by Wang and Xie (1997) and Lawrence and Webster (2002). Both may reflect two extremes of the real phenomenon. It is likely that the strong northward propagation cases picked up by the current study primarily reflect the independent northward propagation scenario, while the weaker northward propagation cases are linked to the Rossby wave emanation scenario in association with equatorial eastward moving ISOs. The proposed mechanisms might be also relevant to the southward propagation in the Southern Hemisphere in boreal winter (see Fig. 2). We will further examine these scenarios in future work.

APPENDIX

Derivation of Linear Governing Equations (1)–(5)

Consider a linear motion in a 2D case (i.e., zonal variation vanishes for all variables) on an f plane. The governing equations under a constant vertical shear in a p coordinate can be written as

Phase speed (ms^{-1}) Growth rate (day^{-1})

FIG. 16. Phase speed (close circle; m s^{-1}) and growth rate (open circle; day^{-1}) of the most unstable modes as a function of vertical shear intensity. The horizontal axis represents the intensity of the easterly shear (i.e., negative $\overline{u}_T$; m s^{-1}).

$$\frac{\partial u}{\partial t} + \omega \frac{\partial \overline{u}}{\partial p} - f_0 v = K \nabla^2 u, \quad \text{(A1)}$$

$$\frac{\partial v}{\partial t} + f_0 u = -\frac{\partial \phi}{\partial y} + K \nabla^2 v, \quad \text{(A2)}$$

$$\frac{\partial v}{\partial y} + \frac{\partial \omega}{\partial p} = 0, \tag{A3}$$

$$\frac{\partial T}{\partial t} + v\frac{\partial \overline{T}}{\partial y} + \omega\frac{\partial \overline{T}}{\partial p} - \frac{1}{\rho C_p}\omega = \frac{\dot{Q}}{C_p} + K\nabla^2 T, \tag{A4}$$

where variables with a bar denote the basic state and variables without a bar denote the ISO perturbation; $\overline{u} = \overline{u}(p)$ is a function of pressure only, $\dot{Q}$ is diabatic heating rate, and K is a diffusivity coefficient.

Writing momentum equations (A1), (A2) on levels 1 and 3, respectively (see Fig. 9 for the model vertical structure), we have

$$\frac{\partial u_1}{\partial t} + \omega_1\left(\frac{\partial \overline{u}}{\partial p}\right)_1 - f_0 v_1 = K\nabla^2 u_1, \tag{A5}$$

$$\frac{\partial u_3}{\partial t} + \omega_3\left(\frac{\partial \overline{u}}{\partial p}\right)_3 - f_0 v_3 = K\nabla^2 u_3, \tag{A6}$$

$$\frac{\partial v_1}{\partial t} + f_0 u_1 = -\frac{\partial \phi_1}{\partial y} + K\nabla^2 v_1, \tag{A7}$$

$$\frac{\partial v_3}{\partial t} + f_0 u_3 = -\frac{\partial \phi_3}{\partial y} + K\nabla^2 v_3. \tag{A8}$$

We further define the barotropic mode as the average of levels 1 and 3 and the baroclinic mode as the difference between the two levels; that is,

$$A_+ = \frac{A_1 + A_3}{2}, \qquad A_- = \frac{A_1 - A_3}{2},$$

where A denotes an arbitrary model variable.

Set $\omega_0 = 0$. The continuity equation (A3) leads to

$$\omega_2 = -D_1\Delta p = -(D_+ + D_-)\Delta p,$$

$$\omega_B = \omega_2 - (D_+ - D_-)\Delta p = -D_+ 2\Delta p,$$

where D denotes the divergence.

Consider a constant vertical shear, $\overline{u}_T = (\overline{u}_1 - \overline{u}_3)/2$, and let $\omega_1 = (\omega_0 + \omega_2)/2$ and $\omega_3 = (\omega_2 + \omega_B)/2$. Equations (A5)–(A8) lead to

$$\frac{\partial u_+}{\partial t} + \overline{u}_T(2D_+ + D_-) - f_0 v_+ = K\nabla^2 u_+, \tag{A9}$$

$$\frac{\partial u_-}{\partial t} - \overline{u}_T D_+ - f_0 v_- = K\nabla^2 u_-, \tag{A10}$$

$$\frac{\partial v_+}{\partial t} + f_0 u_+ = -\frac{\partial \phi_+}{\partial y} + K\nabla^2 v_+, \tag{A11}$$

$$\frac{\partial v_-}{\partial t} + f_0 u_- = -\frac{\partial \phi_-}{\partial y} + K\nabla^2 v_-. \tag{A12}$$

From Eqs. (A9)–(A12), one may derive equations for barotropic and baroclinic vorticity and divergence:

$$\frac{\partial \zeta_-}{\partial t} + f_0 D_- = -\overline{u}_T\frac{\partial D_+}{\partial y} + K\nabla^2\zeta_-, \tag{A13}$$

$$\frac{\partial D_-}{\partial t} - f_0\zeta_- + \nabla^2\phi_- = K\nabla^2 D_-, \tag{A14}$$

$$\frac{\partial \zeta_+}{\partial t} + f_0 D_+ = \overline{u}_T\frac{\partial}{\partial y}(2D_+ + D_-) + K\nabla^2\zeta_+, \tag{A15}$$

$$\frac{\partial D_+}{\partial t} - f_0\zeta_+ + \nabla^2\phi_+ = K\nabla^2 D_+. \tag{A16}$$

Considering a hydrostatic approximation $\partial\phi/\partial p = -RT/p$ and a basic-state thermal wind balance $f_0\, \partial\overline{u}/\partial p = (R/p)\, \partial\overline{T}/\partial y$, the thermal dynamic equation (A4) may be written as

$$\frac{\partial}{\partial t}\left(\frac{\partial \phi}{\partial p}\right) - f_0\frac{\partial \overline{u}}{\partial p}v + S\omega = -\frac{R}{p}\frac{\dot{Q}}{C_p} + K\nabla^2\left(\frac{\partial \phi}{\partial p}\right), \tag{A17}$$

where

$$S = -\frac{R}{p}\frac{1}{\rho g}(\gamma - \gamma_d)$$

is a static stability parameter, $\gamma_d = g/C_p$, and $\gamma = \rho g\partial\overline{T}/\partial p$. Writing Eq. (A17) for the middle troposphere (level 2), we have

$$\frac{\partial \phi_-}{\partial t} - f_0\overline{u}_T v_+ + C_0^2(D_+ + D_-)$$

$$= \frac{R\Delta P}{2P_2 C_p}\dot{Q}_2 + K\nabla^2\phi_-, \tag{A18}$$

where $C_0^2 = \frac{1}{2}S_2(\Delta p)^2$ denotes the square of gravity wave speed for the gravest baroclinic mode.

Assume that the atmospheric heating is proportional to a vertically integrated moisture convergence (Kuo 1974). Hence, we have

$$\dot{Q}_2 = \frac{g}{\Delta p}L_c P_r \quad \text{and}$$

$$P_r = -\frac{b}{g}\int_{P_0}^{P_s}\nabla\cdot(\overline{q}\mathbf{V})\,dp$$

$$= -\frac{b}{g}[\overline{q}_e\nabla\cdot\mathbf{V}_B(p_s - p_e) + \overline{q}_3\nabla\cdot\mathbf{V}_3\Delta p],$$

where P_r is a precipitation rate, $\overline{q}_e$ and $\overline{q}_3$ are vertical mean specific humidity in the PBL and lower troposphere respectively, and b is a heating efficiency coefficient. We have neglected the specific humidity in the upper troposphere.

The precipitation rate may be rewritten as

$$P_r = \frac{b}{g}\Delta p[(2\overline{q}_e - \overline{q}_3)D_+ + \overline{q}_3 D_-]. \tag{A19}$$

Let $q_c = 2C_p P_2 C_0^2/RL_c b\Delta p$, $I = \overline{q}_3/q_c$, and $B = (2\overline{q}_e - \overline{q}_3)/q_c$. We can finally derive the thermal dynamic equation as

$$\frac{\partial \phi_-}{\partial t} - f_0 \overline{u}_T v_+ + c_0^2 (1 - I) D_-$$

$$= c_0^2 (B - 1) D_+ + K \cdot \nabla^2 \phi_- . \qquad (A20)$$

In the equation above, I and B are heating coefficients proportional to specific humidity in the lower troposphere and PBL, and terms $c_0^2 (1 - I) D_-$ and $c_0^2 (B - 1) D_+$ represent convective heating due to moisture convergence in the free atmosphere and frictional moisture convergence in the PBL, respectively. Equations (A13)–(A16) and (A20) form a simple dynamic framework for mechanism discussions in section 4.

REFERENCES

Cadet, D. L., 1986: Fluctuations of precipitable water over the Indian Ocean. *Tellus,* **38A,** 170–177.

Goswami, B. N., and J. Shukla, 1984: Quasiperiodic oscillations in a symmetric general circulation model. *J. Atmos. Sci.,* **41,** 20–37.

Kemball-Cook, S. R., and B. Wang, 2001: Equatorial waves and air–sea interaction in the boreal summer intraseasonal oscillation. *J. Climate,* **14,** 2923–2942.

Krishnamurti, T. N., and D. Subrahmanyam, 1982: The 30–50-day mode at 850 mb during MONEX. *J. Atmos. Sci.,* **39,** 2088–2095.

Kuo, H.-L., 1974: Further studies of the parameterization of the influence of cumulus convection on large-scale flow. *J. Atmos. Sci.,* **31,** 1231–1240.

Lau, K.-M., and P. H. Chan, 1986: Aspects of the 40–50 day oscillation during the northern summer as inferred from outgoing longwave radiation. *Mon. Wea. Rev.,* **114,** 1354–1367.

Lawrence, D. M., and P. J. Webster, 2002: The boreal summer intraseasonal oscillation: Relationship between northward and eastward movement of convection. *J. Atmos. Sci.,* **59,** 1593–1606.

Li, T., 1997: Air–sea interactions of relevance to the ITCZ: The analysis of coupled instabilities and experiments in a hybrid coupled GCM. *J. Atmos. Sci.,* **54,** 134–147.

——, and B. Wang, 1994: The influence of sea surface temperature on the tropical intraseasonal oscillation: A numerical experiment. *Mon. Wea. Rev.,* **122,** 2349–2362.

Lorenc, A. C., 1984: The evolution of planetary scale 200mb divergences during the FGGE year. *Quart. J. Roy. Meteor. Soc.,* **110,** 427–441.

Madden, R. A., and P. R. Julian, 1971: Detection of a 40–50 day oscillation in the zonal wind in the tropical Pacific. *J. Atmos. Sci.,* **28,** 702–708.

——, and ——, 1972: Description of global-scale circulation cells in the Tropics with a 40–50 day period. *J. Atmos. Sci.,* **29,** 3138–3158.

Murakami, T., T. Nakazawa, and J. He, 1984: On the 40–50 day oscillations during the 1979 Northern Hemisphere summer. I: Phase propagation. *J. Meteor. Soc. Japan,* **62,** 440–468.

Nordeng, T. E., 1994: Extended versions of the convective parameterization schemes at ECMWF and their impact on the mean and transient activity of the model in the Tropics. ECMWF Tech. Memo. 206, 41 pp.

Roeckner, E., and Coauthors, 1996: The atmospheric general circulation model ECHAM-4: Model description and simulation of present-day climate. Max Planck Institut für Meteorologie Rep. No. 218, Hamburg, Germany, 90 pp.

Sikka, D. R., and S. Gadgil, 1980: On the maximum cloud zone and the ITCZ over Indian longitudes during the southwest monsoon. *Mon. Wea. Rev.,* **108,** 1840–1853.

Tiedtke, M., 1989: A comprehensive mass flux scheme for cumulus parameterization in large-scale models. *Mon. Wea. Rev.,* **117,** 1779–1800.

Wang, B., and H. Rui, 1990: Synoptic climatology of transient tropical intraseasonal convection anomalies: 1975–1985. *Meteor. Atmos. Phys.,* **44,** 43–61.

——, and T. Li, 1993: A simple tropical atmospheric model of relevance to short-term climate variation. *J. Atmos. Sci.,* **50,** 260–284.

——, and ——, 1994: Convective interaction with boundary-layer dynamics in the development of a tropical intraseasonal system. *J. Atmos. Sci.,* **51,** 1386–1400.

——, and X. Xie, 1997: A model for the boreal summer intraseasonal oscillation. *J. Atmos. Sci.,* **54,** 72–86.

Webster, P. J., 1983: Mechanisms of low-frequency variability: Surface hydrological effects. *J. Atmos. Sci.,* **40,** 2110–2124.

Xie, P., and P. A. Arkin, 1997: Global precipitation: A 17-year monthly analysis based on gauge observations, satellite estimates and numerical model outputs. *Bull. Amer. Meteor. Soc.,* **78,** 2539–2558.

Xie, S.-P., and S. G. H. Philander, 1994: A coupled ocean–atmosphere model of relevance to the ITCZ in the eastern Pacific. *Tellus,* **46A,** 340–350.

Yasunari, T., 1979: Cloudiness fluctuations associated with the Northern Hemisphere summer monsoon. *J. Meteor. Soc. Japan,* **57,** 227–242.

——, 1980: A quasi-stationary appearance of 30- to 40-day period in the cloudiness fluctuations during the summer monsoon over India. *J. Meteor. Soc. Japan,* **58,** 225–229.